Optimization of a convex pattern surface for sliding wear reduction based on a definitive screening design and discrete element method

Yan, Yunpeng; Helmons, Rudy; Wheeler, Craig; Schott, Dingena

Important note
To cite this publication, please use the final published version (if applicable).
Please check the document version above.

Optimization of a convex pattern surface for sliding wear reduction based on a definitive screening design and discrete element method

Yunpeng Yan [a],*, Rudy Helmons [a], Craig Wheeler [b], Dingena Schott [a]

[a] Department of Maritime and Transport Technology, Delft University of Technology, 2628, CD, Delft, the Netherlands
[b] School of Engineering, The University of Newcastle, Callaghan 2308, Australia

ARTICLE INFO

ABSTRACT

A previous study revealed that a convex pattern surface can reduce sliding wear of a transfer chute. A convex pattern surface is a flat surface outfitted with a pattern of convexes defined by five parameters. A three-level definitive screening design (DSD) method combined with discrete element method (DEM) is used to investigate the influence of the five parameters and two operational conditions on the sliding wear. Two flow regimes are distinguished, namely continuous and discontinuous flow regimes, and both flow regimes can significantly reduce the sliding wear. The particle velocity and angular velocity profiles verify the guiding and rolling effect of the convex pattern on the motion of particles. A regression model fitted based on the DSD indicates that three main factors and one interaction have significant influence on the sliding wear.

© 2021 Published by Elsevier B.V.

1. Introduction

Bulk solids handling plays a significant role in a range of industries, such as the mining, agricultural, chemical, and pharmacology industries [1]. For the mining industry, the process of transferring bulk solids, e.g. iron ore, leads to surface wear of handling equipment. Two principal wear mechanisms can be distinguished: abrasive wear and erosive (impact) wear [2,3]. Studies show that approximately 82% of the energy loss is attributed to the bulk material sliding along the chute bottom and 9% of the losses due to sliding against the side walls [4]. Severe wear has been found in several locations on bulk handling equipment, for example silo walls and transfer chute bottom sections [4,5]. Wear leads to surface deformation and volume loss of handling equipment and accelerates the damage of the equipment, resulting in a reduction of lifespan. The maintenance of wear areas is costly and generally increases downtime. To save costs and reduce downtime, the surface wear of bulk solids handling equipment must be reduced.

Traditional methods to reduce surface wear of bulk solids handling equipment relies on five aspects [6]: (1) optimizing operational conditions based on theoretical wear models [4,7]; (2) using wear-resistant materials with coating technologies [8]; (3) supplying a repulsive force to diminish the contact force between particulate solids and equipment [1]; (4) adding assistant components by using the self-wear mechanism of the bulk solids [8]; and (5) fabricating a surface geometry pattern to affect the kinematics of the bulk material flowing along the surface [9,10]. In this research, a geometry pattern equipped on a smooth surface is studied based on a bionic design [11]. Scientists have discovered several surface morphologies [12–14] that can achieve lower wear rates compared to smooth surfaces [15–17], and recently a convex pattern surface was introduced to reduce the sliding wear of transfer chutes [18,19]. However, the effects of geometrical parameters of a convex pattern and operational conditions, such as bulk velocity and particle bed height, on the sliding wear, are still uncertain.

This paper aims at optimizing a convex pattern surface for sliding wear reduction through the discrete element method (DEM). First, the critical factors of the convex pattern and the selected operational conditions are sorted out based on a definitive screening design (DSD). Second, the relationship between the bulk flow regimes and the factors is investigated. Third, the mechanisms of the sliding wear reduction are elaborated based on contact behavior between particles and samples.

2. Discrete element method

2.1. DEM contact model

Discrete element method (DEM) is developed by Cundall and Strack [20] to model particle systems by tracking the movement of each particle and interaction with its surroundings over time. DEM is the most attractive computational method used by researchers and engineers to successfully design, analyze, and optimize bulk materials handling systems and equipment for granular materials [21,22].

* Corresponding author.
E-mail address: Y.Yan@tudelft.nl (Y. Yan).

The motion of discrete particles in DEM is governed by Newton's second law of motion [21]. The Hertz-Mindlin no-slip contact model, shown in Fig. 1, is a nonlinear elastic contact model [23] which is appropriate for non-cohesive granular materials. This model consists of two springs, two dampers, and a slider. The springs are used to represent particle stiffness in normal and tangential directions. Two dampers are used to model the damping forces, and the slider is applied to generate a friction force. In this study, a DEM software package EDEM 2018.1 [24] is used. The normal force F_n is calculated according to Eq. (1), where S_n, δ_n, D_n, and v_n are the stiffness, overlap, coefficient of restitution, and velocity in the normal direction of the contact, respectively.

$$F_n = -\frac{2}{3}S_n\delta_n^{\frac{1}{2}} + D_n v_n \tag{1}$$

The tangential force F_t is restrained by Coulomb law [25], which is expressed by Eq. (2), where μ_{st} is the coefficient of static friction; S_t, δ_t, D_t, and v_t are the stiffness, overlap, coefficient of damping force, and velocity in the tangential direction of the contact, respectively.

$$F_t = \min\{-S_t\delta_t + D_t v_t, \mu_{st}F_n\} \tag{2}$$

Spherical particles are normally used to study wear process since DEM is an expensive technique for modeling particulate systems at the individual particle scale [26]. In this study we use spherical particles based on findings of previous studies. These have shown that using spherical particles can reach a good agreement with experimental results. For example, Esteves et al. [27] compared a vertical stirred mills screw liner wear (wear profile and wear volume) after more than 3000 h test with simulation results (spherical particles and Archard wear model). For other applications, such as ball mill liner wear, spherical particles were used to predict the wear of mill based on DEM simulations [28–30].

The non-spherical particle shape is accounted for by the use of a rolling friction model [31,32]. A review of rolling friction identified four different classes of rolling resistance models that are commonly used in DEM [33]. In this study, rolling type A is chosen because it is effective for modeling small scale systems such as sandpile formation and can also be used for rolling energy dissipation in a dynamic scenario if the adopted computational time step is sufficiently small [33]. Type A applies a constant torque on a particle to represent rolling friction, and the direction of the torque is always against the relative rotation between two contact entities. This mechanism can also be applied to contact between particles. A typical model of rolling model Type A by Zhou [34] is expressed by Eq. (3)

$$M_r = -\frac{\omega_{rel}}{|\omega_{rel}|}\mu_r R_r F_n \quad (a) \tag{3}$$
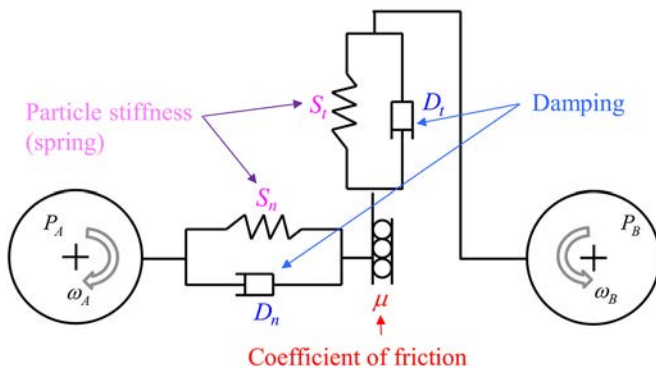
$$\omega_{rel} = \omega_i - \omega_j \quad (b)$$

Fig. 1. Hertz-Mindlin no-slip contact model.

where M_r is the torque between two in-contact disks i and j. ω_i and ω_j are the angular velocities of disks i and j, respectively, and ω_{rel} is the relative angular velocity between them.

To ensure realistic behavior of the bulk material, calibration of the sliding and rolling friction coefficients has been performed in this study. Laboratory scale experiments were executed to determine characteristic behavior of the material. These experimental results were used to calibrate the material to confirm the ability of the DEM material model to capture the material behavior realistically. A detailed description of the calibration can be found in Section 3.

2.2. Sliding wear model

Archard wear model [35] is applied to calculate the wear volume caused by the sliding of particles. This wear model has been widely used for bulk handling process, such as the prediction of the wear of mill lifters [36] and local failure prediction of abrasive wear on tipper bodies [37]. Eq. (4) shows the generalized equation to calculate sliding wear volume.

$$W_v = k\frac{F_n}{H_s}l_s \tag{4}$$

where $W_v(mm^3)$ is the wear volume, H_s (N/mm^2) is the hardness of the surface, k is a dimensionless wear coefficient, $F_n(N)$ is the normal force applied to an equipment surface, and $l_s(mm)$ is the sliding distance. By introducing the coefficient of sliding wear α_s in Eq. (5),

$$\alpha_s = \frac{k}{H_s} \tag{5}$$

Eq. (4) is simplified as Eq. (6).

$$W_v = \alpha_s F_n l_s \tag{6}$$

3. Calibration of DEM parameters

3.1. Experiments

River gravel is used in this research, and this material is classified as dry, non-cohesive, and free-flowing. A sample of the river gravel is shown in Fig. 2, and the particle size distribution is given in Fig. 3.

The shear box test (Fig. 4) and drawdown test (Fig. 5) were executed at The University of Newcastle, Australia, to characterize the relevant bulk properties. The shear box is made of Perspex with dimensions of 200 mm by 200 mm by 200 mm. In the experiment, a total mass of 11.64 kg of river gravel is poured into the box to a filling height of 200 mm. After the preparation, the right wall is opened, and the remaining gravel forms a slope. The angle of the slope is called shear angle. The test was conducted three times for repeatability.

The box of the drawdown test is made of two kinds of materials which are Perspex for front and back walls and steel for side walls. The upper box and lower box have the identical dimensions with length of 500 mm, width of 100 mm, and height of 500 mm. A square opening is positioned at the bottom center which can be opened to allow the discharge of the bulk material. A total mass of 19.68 kg of the river gravel fills a height of 280 mm in the upper box. The outflowing bulk material forms a pile in the lower box, while the remaining bulk material forms two slopes in the upper box. In addition, the test allows the measurement of the discharge time during the experiment. After the measurement of discharge time T_d, the shear angle α_{DD} and angle of repose β_{DD} are determined. The test is performed three times for repeatability.

Fig. 4 and Fig. 5 show the examples of the shear box test and drawdown test. The experimental results are summarized in Table 1. For the shear box test, the averaged shear angle of the shear box test was determined as 36.0 ± 0.4 degrees. For the drawdown test, the averaged shear
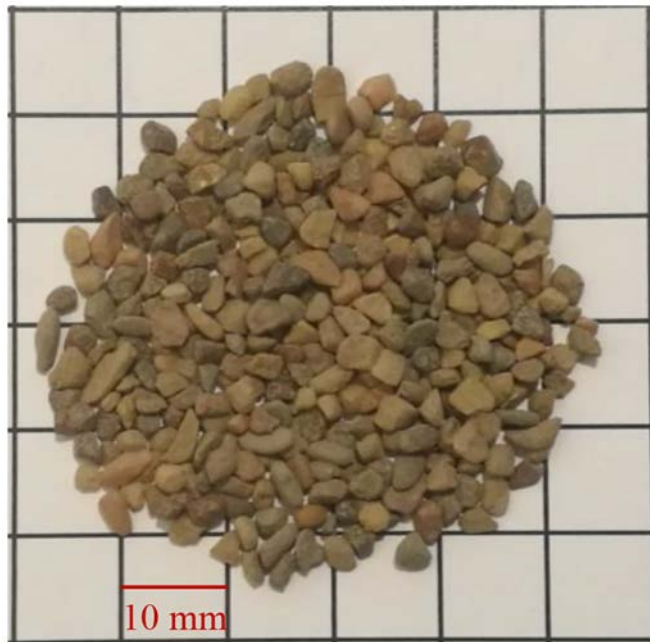
Fig. 2. Sample of river gravel.

Fig. 4. Shear angle in the shear box test.

angle and angle of repose are 36.1 ± 0.5 and 33.3 ± 0.9 degrees respectively. In addition, the averaged discharge time is 5.4 ± 0.1 seconds.

3.2. DEM calibration

As shown in Fig. 3, the particles with diameter smaller than 2 mm account for 0.26% of the total mass. In order to save computational time, the particles with a size lower than 2 mm are neglected in DEM simulations.

Based on literature review [37–39], the coefficient of sliding friction $\mu_{s,p-p}$ and the coefficient of rolling friction $\mu_{r,p-p}$ between particles are the most influential parameters on bulk flow properties, so these two parameters are calibrated. The other parameters of the DEM model are given in Table 2. The particle solids density is calibrated by the drawdown test in the filling process since the shear angle for the shear box test is not sensitive to the particle solids density [38].

The shear box test is performed first to get a rough range of possible combinations of these two parameters because this test needs less computational time compared with the drawdown test. To reduce the computational time, the effect of the box dimensions is investigated. Based
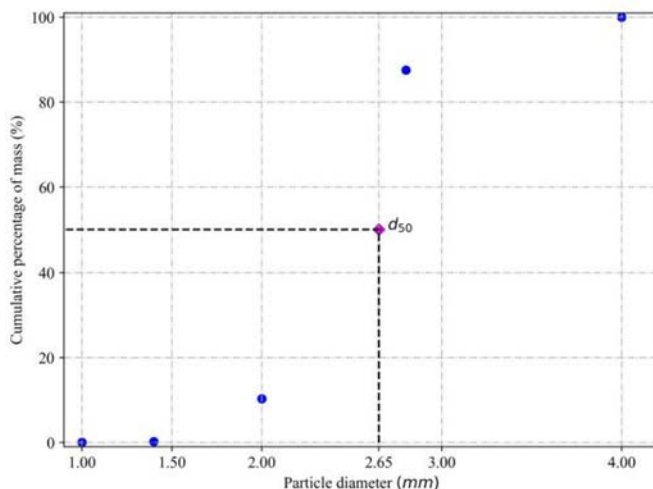
Fig. 3. Particle size distribution.

Fig. 5. Shear angle and angle of repose in the drawdown test.

Table 1
Summary of the experimental results.

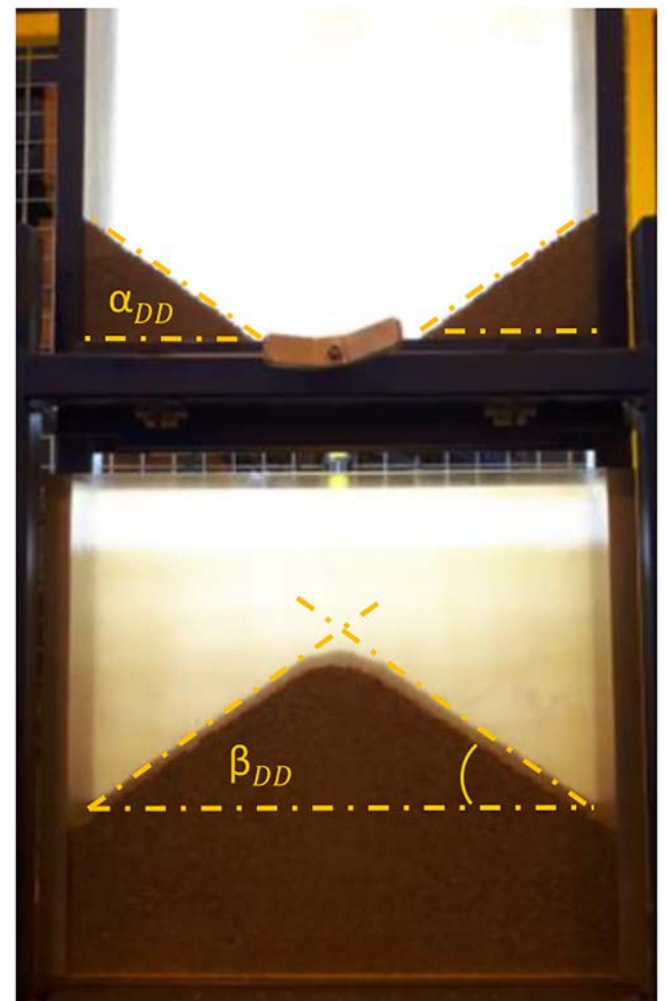| Experiment	Measured variable	Value
Shear box	α_{SB}	$36 \pm 0.4°$
Draw down test	α_{DD}	$36.1 \pm 0.5°$
	β_{DD}	$33.3 \pm 0.9°$
	T_d	$5.4 \pm 0.1 s$

Table 2
General DEM parameters.

Categories	Parameters	Values
Contact model	–	Hertz-Mindlin (no slip)
Rolling friction model	–	Type A
	Particle density (kg/m^3)	2460
River sand	Poisson ratio $\nu\,(-)$	0.24
	Shear modulus $G\,(GPa)$	0.07
	Density (kg/m^3)	1200
Perspex	Poisson ratio $\nu\,(-)$	0.5
	Shear modulus $G\,(GPa)$	0.1
	Density (kg/m^3)	7932
Steel	Poisson ratio $\nu\,(-)$	0.3
	Shear modulus $G\,(GPa)$	78
Particle-particle	Coefficient of restitution	0.45
	Coefficient of restitution $(-)$	0.4
Particle-perspex	Coefficient of static friction $(-)$	0.36
	Coefficient of rolling friction $(-)$	0.36
	Coefficient of restitution $(-)$	0.6
Particle-steel	Coefficient of static friction $(-)$	0.38
	Coefficient of rolling friction $(-)$	0.3
Time step	$\Delta t\,(s)$	$5e - 6$
Gravitational acceleration	m/s^2	9.81

on [26], a similar shear angle is obtained when the width of the shear box is four times larger than the particle diameter with a periodic boundary condition. Considering the d_{50} of the river gravel is 2.65 mm, as shown in Fig. 3, the width of the box is set as 20 mm under the application of periodic boundary conditions. In the test, both the coefficients of sliding and rolling friction are set at 0.24. Three sizes are evaluated, and each test is repeated three times. The results listed in Table 3 show the shear angle of the shear box with a dimension of 100 mm by 100 mm can obtain a comparable result to that of 200 mm by 200 mm.

After the investigation of the effect of the dimensions of the container on the shear angle, the shear box test is performed for a range of coefficients of sliding and rolling friction listed in Table 4. Sixteen simulations are conducted, and Fig. 6 shows the shear angle as a function of sliding and rolling friction between particles. It can be seen that multiple combinations of these two coefficients result in the same shear angles, as shown in Fig. 6. The area from 36° to 38° represents the potential combinations to match the experimental results.

For the drawdown test (see Fig. 5), the width of the box is set as 60 mm because when the width of the box is higher than 20 times the particle diameter, the wall effect can be neglected [39]. This means the shear angle, angle of repose, and discharge time are only determined by the contact parameters. To obtain the final combination, two steps are used for the drawdown test. First, a wide range of $\mu_{s,p-p}$ from 0.2

Table 3
Simulation results of shear box test.

Dimension (mm^3)	Averaged $\alpha_{SB}(°)$	Deviation (°)
$200 \times 200 \times 20$	31.2	0.9
$150 \times 150 \times 20$	30.4	0.5
$100 \times 100 \times 20$	31.1	0.7

Table 4
Coefficients of sliding and rolling friction in DEM simulations.

$\mu_{s,p-p}$	0.2	0.4	0.6	0.8
$\mu_{r,p-p}$	0.1	0.3	0.5	0.7
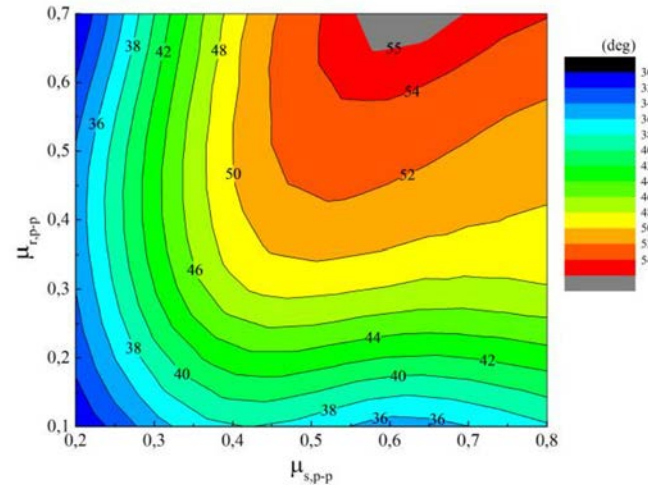
Fig. 6. Shear angle results of shear box test.

to 0.7 is investigated to obtain a narrow scope. Second, a detailed investigation is conducted at this narrow scope.

Table 5 lists the selection of the combinations for the first step. As explained in [38], the coefficient of static friction determines the discharge time and increasing the coefficient of static friction reduces the mass flow rate and increases the discharge time. In contrast, the coefficient of rolling friction has minor influence on the discharge time. Therefore, the coefficient of static friction should be lower than 0.3 to guarantee a faster discharge.

For the second step, the value of $\mu_{s,p-p}$ is selected at a range of 0.21 to 0.29 with an interval of 0.01 and the corresponding $\mu_{r,p-p}$ is chosen from Fig. 6. Finally, a combination of (0.21, 0.4) $(\mu_{s,p-p}, \mu_{r,p-p})$ satisfies the experimental results, as shown in Table 6.

4. Experimental design for simulations

4.1. Simulation setup

A convex pattern surface as shown in Fig. 7 can be described by five parameters [11,18]: major and minor radii a and b, vertical and horizontal distance c and d, and height of the convex h. To ensure that the sliding wear happens only on the top surface, the sample is covered by a holder. The sample is meshed using Ansys Workbench 18.2 [40]. It should be noted that the sliding wear does not remove the meshes, and the sample keeps intact during the simulation.

Table 5
Selection of combinations.

Run	$\mu_{s,p-p}$	$\mu_{r,p-p}$	$\beta_{DD}(°)$	$\alpha_{DD}(°)$	$T_d(s)$
1	0.2	0.45	35.1	35.5	6.2
2	0.3	0.15	36.9	37.6	10.5
3	0.5	0.1	26.3	36.0	12.3
4	0.6	0.12	37.5	38.8	11.1
5	0.7	0.1	28.0	36.9	10.9

Table 6
Comparison between experimental and simulation results.

Test	Criteria	Experimental result	Simulation result
Shear box	$\alpha_{SB}(°)$	36±0.4	35.7
	$\alpha_{DD}(°)$	36.1±0.5	36.3
Draw down test	$\beta_{DD}(°)$	33.3±0.9	34.3
	$T_d(s)$	5.4±0.1	5.6

In terms of operational conditions, the normal load [41] and the relative velocity [42,43] have significant effect on the sliding wear. The normal load is directly related to the particle bed thickness, which is defined by the depth of the particle bed, so particle bed thickness is selected as an operational condition. The velocity of the sample is achieved by applying a constant velocity to the sample in y-direction. Fig. 8 shows a particle bed clipped from the middle (thickness t) with dimensions of 2000 mm by 300 mm The sample with the dimensions of 200 mm by 200 mm is located at the left bottom center of the particle bed and moves in y-direction with a velocity v.

The central and side bins are linked to and move with the sample to investigate the contact behavior between particles and the sample, as shown in Fig. 9. The dimensions of the central and side bins are 200 mm by 200 mm and 200 mm by 50 mm, respectively. The moving bins consist of multiple layers from the bottom to the surface of the particle bed, and the thickness of each layer is set as 5 mm.

### 4.2. Definitive screening design (DSD)

Screening design is a major use of fractional factorial design [44], which is used to identify the factors that affect the response. In this research, the response, which is the dependent variable, is the sliding wear volume, and the independent variables are the six factors mentioned in Section 4.1. A three-level definitive screening design is applied to this research, as it is able to assess the curvature of the factor-response relationship [45]. For the screening design, the independent factors should be at a wide but reasonable range [44]. Therefore, level 2 is two times higher than level 1, and level 3 four times higher than level 1 except for the horizontal distance d. Considering the particle size distribution, the level 1 of the major and minor radii are set as 2 mm. To guarantee the space between two convexes, the horizontal distance should be at least two times higher than the minor radius, so level 1 of d is set as 20 mm. The horizontal distance d is increased by 20 mm from level 1 to level 3. The vertical distance c has no influence on the sliding wear reduction [11] and is therefore kept constant as 40 mm. Table 7 lists the factors and the corresponding levels.

Table 8 shows the three-level definitive screening design pattern. The columns of the design are orthogonal to each other if the level 1, 2, and 3 are regarded as −1, 0, and 1, respectively, which means that in the list of test runs, the levels of each factor occur an equal number of times with each of the levels of the other factors. This design ensures that the estimated factor effects are statistically independent [45].

4.3. Analysis procedure

The analysis of the wear results should be based on the steady state of the simulation setup. Therefore, the stability of the simulation setup is evaluated first. In order to verify that the convex pattern surface can reduce the sliding wear, the simulations with flat surfaces under corresponding operational conditions listed in Table 8 are performed as references.
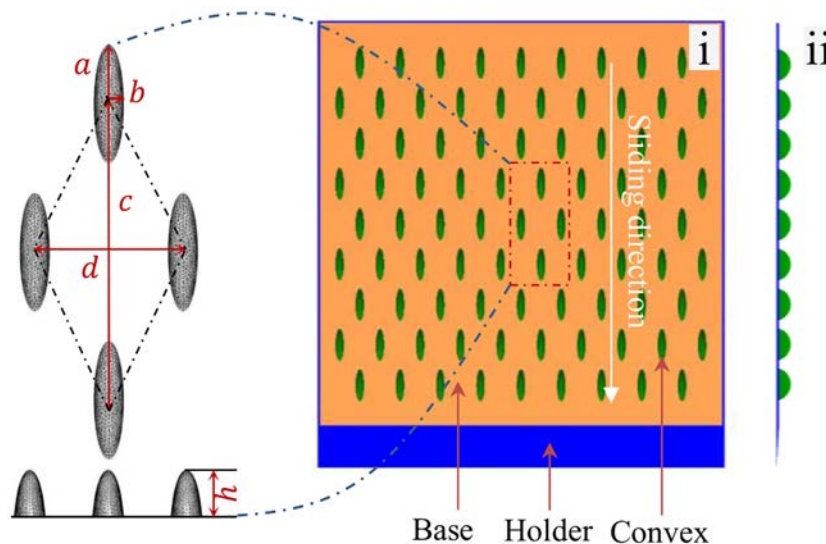
Fig. 7. Meshed convex pattern surface based on [18] i): top view; ii): side view (a: major radius; b: minor radius; c: vertical distance; d: horizontal distance; h: height of convex).
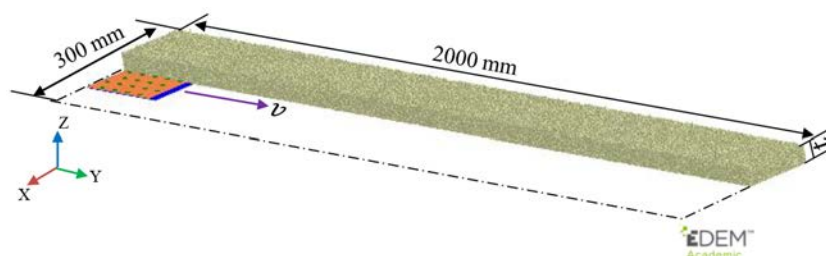
Fig. 8. Simulation setup (clipped from the middle of the particle bed with v sample velocity, t particle bed thickness).
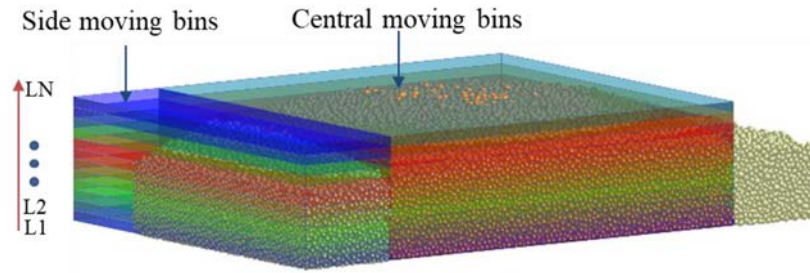
Fig. 9. Setting of moving bins (clipped from the middle of the sample).

Table 7
Six factors at three levels for screening design.

Factors	Levels		
	Minimum (-1)	Middle (0)	Maximum (1)
a (major radius/mm)	2	4	8
b (minor radius/mm)	2	4	8
d (horizontal distance/mm)	20	40	60
h (height/mm)	1.5	3	6
v (sample velocity/m/s)	0.5	1	2
t (bed thickness/mm)	10	20	40

The stability of the sliding process includes two aspects: the bulk flow steady state and the sliding wear stability. Two criteria are used to evaluate the stability of the sliding process: relative velocity of bulk material and relative wear gradient of samples.

For the relative velocity of bulk material, it is considered that the particle flow is at steady state when the ratio of the averaged particle velocity at the sample moving direction (y-direction) to the sample velocity reaches a relatively steady value. It should be noted that only the particles in the central moving bins (see Fig. 9) with the original particle bed height are considered for this criterion. The relative velocity η is defined as

$$\eta = \frac{\overline{v_p}}{v_s} \times 100\% \tag{7}$$

where η is relative velocity, $\overline{v_p}$ is averaged particle velocity in sample moving direction, and $v_s(mm/s)$ is the translational velocity of the sample.

Relative wear gradient φ_R is used to evaluate the stability of the sliding wear process, which is denoted by Eq. (8).

Table 8
Three-level definitive screening design for six factors.

Run order	Run Pattern	Factors					
		a	b	d	h	v	t
R1	$+0+--+$	8	4	60	1.5	0.5	40
R2	$-++-0-$	2	8	60	1.5	1.0	10
R3	$+-+0+-$	8	2	60	3.0	2.0	10
R4	$0-----$	4	2	20	1.5	0.5	10
R5	$0+++++$	4	8	60	6.0	2.0	40
R6	000000	4	4	40	3.0	1.0	20
R7	$++0+--$	8	8	40	6.0	0.5	10
R8	$-+-0-+$	2	8	20	3.0	0.5	40
R9	$+--+0+$	8	2	20	6.0	1.0	40
R10	$--++-0$	2	2	60	6.0	0.5	20
R11	$-0-++-$	2	4	20	6.0	2.0	10
R12	$++--+0$	8	8	20	1.5	2.0	20
R13	$--0-++$	2	2	40	1.5	2.0	40

$$\varphi_R = \frac{\varphi}{\max(\varphi)} \tag{8}$$

where φ_R is relative wear gradient, $\varphi(mm^3/mm)$ is wear gradient, and $\max(\varphi)(mm^3)$ is the maximum value of wear gradient of all simulations.

The wear gradient φ is denoted by Eq. (9).

$$\varphi = \frac{W_{v,s} - W_{v,s-\Delta s}}{\Delta s} \tag{9}$$

where $\varphi(mm^3/mm)$ is wear gradient, $\Delta s(mm)$ is displacement increment of the sample, and $W_{v,s} - W_{v,s-\Delta s}(mm^3)$ is wear volume increment.

After the analysis of the stability of the simulation setup, the sliding wear result is investigated. A relative wear volume is used to compare the sliding wear for Group A and Group B separately, and the groups are elaborated in Section 5.1.

The relative wear rate γ is defined by Eq. (10).

$$\gamma = \frac{w_{v,convex}}{\max\{w_{v,convex}, w_{v,flat}\}} \tag{10}$$

where γ is relative wear rate, $w_{v,convex}$ (m^3) and $w_{v,flat}(m^3)$ are the wear volumes of the convex sample and corresponding flat surface, respectively. $\max\{w_{v,convex}, w_{v,flat}\}$ is the maximum value in each group.

The wear rate w_r is denoted by Eq. (11).

$$w_v = \frac{W_v}{m} = \frac{W_v}{v \times t \times l \times \rho} \tag{11}$$

where $w_v(m^3/(kg/s))$ is wear rate, W_v (m^3) is wear volume, $m(kg/s)$ is mass flow rate, $v(m/s)$ is the sample velocity, t (m) is the thickness of particle bed, l (m) is the width of the particle bed, and $\rho(kg/m^3)$ is the bulk density.

5. Results

5.1. Steady state evaluation

Fig. 10 shows the relative velocities of the thirteen simulations. These simulations are separated into two groups (Group A and B) based on the two bulk flow regimes, as shown in Fig. 11. The flow regime Group A in Fig. 11 (a) shows that the particle bed fully covered by particles after the travel of the sample and this flow regime is called continuous flow regime. The flow regime of Group B as shown in Fig. 11 (b) illustrates that the sample forces the particles to move with the sample as the relative velocity close to 1, leading to particle accumulation. Therefore, this flow regime is named discontinuous flow regime.

The flow regimes can significantly influence the relative particle velocities. The continuous flow regime of Group A as shown in Fig. 10 has a relatively wide range of ratios from 15% to 70%. It can be divided into three subgroups because the simulation runs in those subgroups have
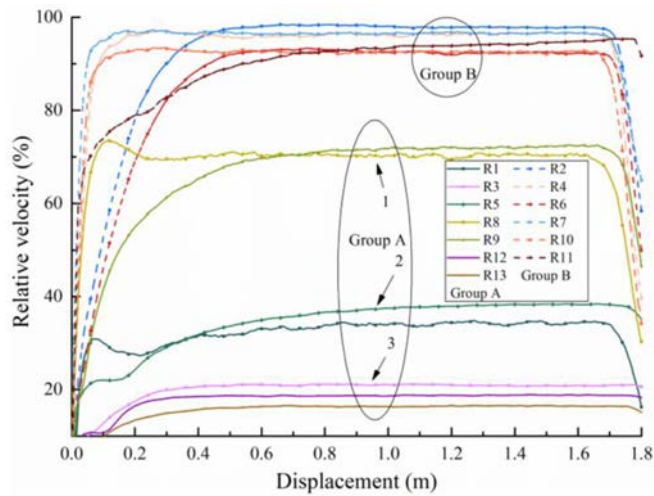
Fig. 10. Relative velocity of particles.

common factors. For Group A1, the common factors are the horizontal distance (20 mm) and the particle bed thickness (40 mm). Group A2 has the same horizontal distance (60 mm) and the particle bed thickness (40 mm). Group A3 has the identical sample velocity (2 m/s). For the discontinuous flow regime of group B, the relative velocity is close to 100%, which means the particles move with the sample at a close velocity, and this result is consistent with the flow regime shown in Fig. 11 (b).

For all simulations, the relative velocities increase rapidly at the first 200 mm and get into a transitional state from 200 mm to 800 mm. Finally, all simulations reach a steady state from 800 mm to 1700 mm with fluctuations less than 7%. The fluctuations occur because the

particle bed height is always changing with the movement of the sample, so the averaged particle velocity changes and leads to the fluctuation of the relative velocity.

Fig. 12 shows the relative wear gradient of all simulations, and these simulations are divided into two groups based on the flow regimes shown in Fig. 11. It can be seen that the continuous flow regime of Group A (including Group A1, A2, and A3) has significant higher relative wear gradient than the discontinuous flow regime of Group B, which means the wear gradient is closely related to the bulk flow regimes. Group B shows a relatively high fluctuation, and all simulations have fluctuation of less than 0.002. The possible reason is that the discontinuous flow regime of Group B causes the particles to accumulate on and in front of the sample, so the accumulated particles influence the contact force between particles and the sample, therefore increasing sliding wear.

For all simulations, the relative wear gradient decreases rapidly at the first 200 mm and goes into a transitional state until 1000 mm. Finally, all simulations obtain a steady state from 1000 mm to 1700 mm. Combining the two stability criteria, all simulations reach a steady state from 1000 mm to 1700 mm, and the wear results are closely related to the flow regimes; so, the analysis of results is performed at the steady state separately, based on the two flow regimes.

5.2. Sliding wear

Fig. 13 shows the relative wear rate of the two flow regimes indicated by Group A and B. Within the continuous flow regime of Group A, all convex surfaces except R12 can reduce the sliding wear, as shown in Fig. 13 (a). The sample of the R12 is almost fully covered by the convexes based on Table 8, so the majority of the sliding wear appears at the convexes. This shows wrong combinations of the factors
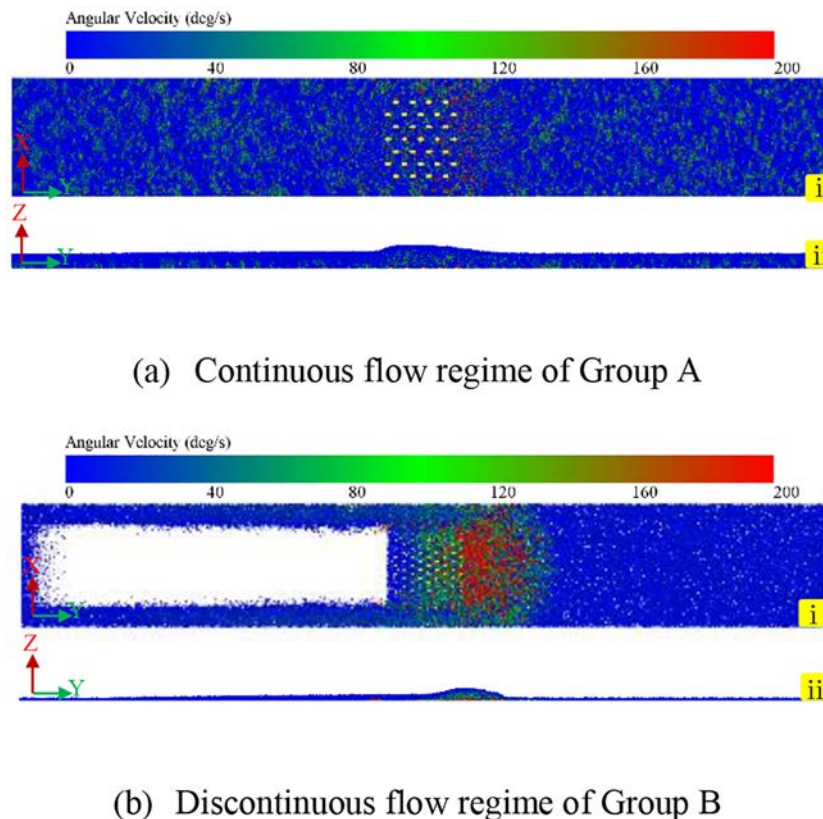

(a)　Continuous flow regime of Group A

(b)　Discontinuous flow regime of Group B

Fig. 11. Bulk flow regimes with i) bottom view (x-y direction), ii) side view (y-z direction).
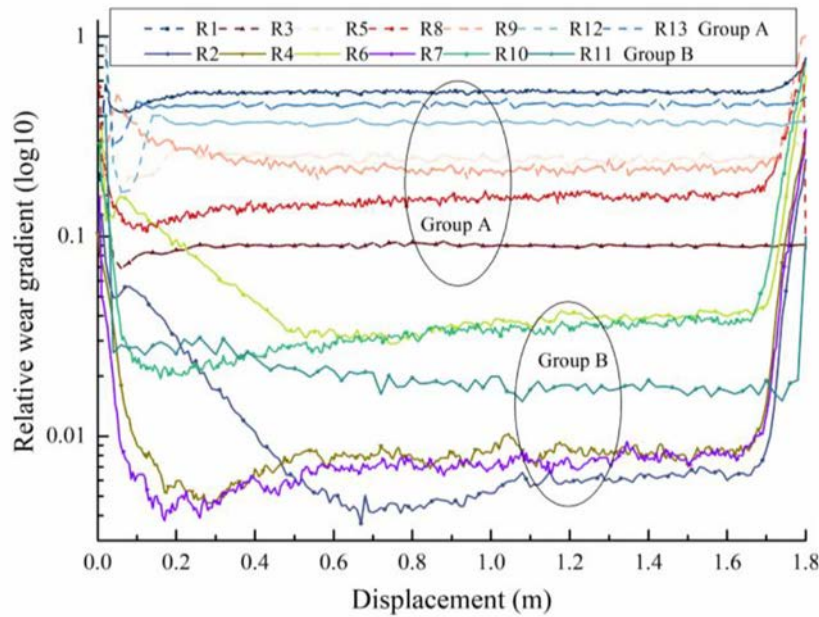
Fig. 12. Relative wear gradient.

could increase the sliding wear. The other runs shows that the bases of the samples have higher proportions of the sliding wear compared with the convexes. R5 has the lowest relative wear rate and reduces the sliding wear by 66% compared with the corresponding flat surface. Fig. 13 (b) shows the convex pattern surfaces of the discontinuous flow regime can reduce the sliding wear compared to the flat surfaces, and the sliding wear occurs mainly on the sample bases. R2 has the lowest relative wear and reduces the sliding wear by 17% compared with the corresponding flat surface. As the R5 (Group A) and R2 (Group B) have the lowest relative wear rates for these two flow regimes, they are selected for detailed analysis to reveal the bulk flow properties.

Figs. 14 and 15 illustrate the sliding wear distributions of the convex pattern and flat surfaces. Fig. 14 shows the wear distributions of the samples of R5 and the corresponding flat surface. For the base of the R5 in Fig. 14(a), the majority of the sliding wear appears at the front

two rows of the convexes and the two sides of the sample. The reason lies in that the sliding distance of particles at the front part is much longer than that of the back part. For detailed explanation, please view the Appendix A. The wear path on the base indicates the guiding effect of the convex pattern as the particles contacting with the base are directed sideways and move around the convexes. For the convex pattern, as shown in Fig. 14(a), the majority of wear appears at the front half part because contact between particles and the convex mainly appears at this area. Fig. 14(b) shows the wear distribution of the corresponding flat surface. It is obvious that the sliding path is along the sample moving direction and the front part of the sample shows lower sliding wear than the back part. The reason lies in that the normal force in the front part is relatively lower than the rest of the part because the accumulation of particles over the sample is more obvious. For detailed explanation of Fig. 14, please see Appendix A.
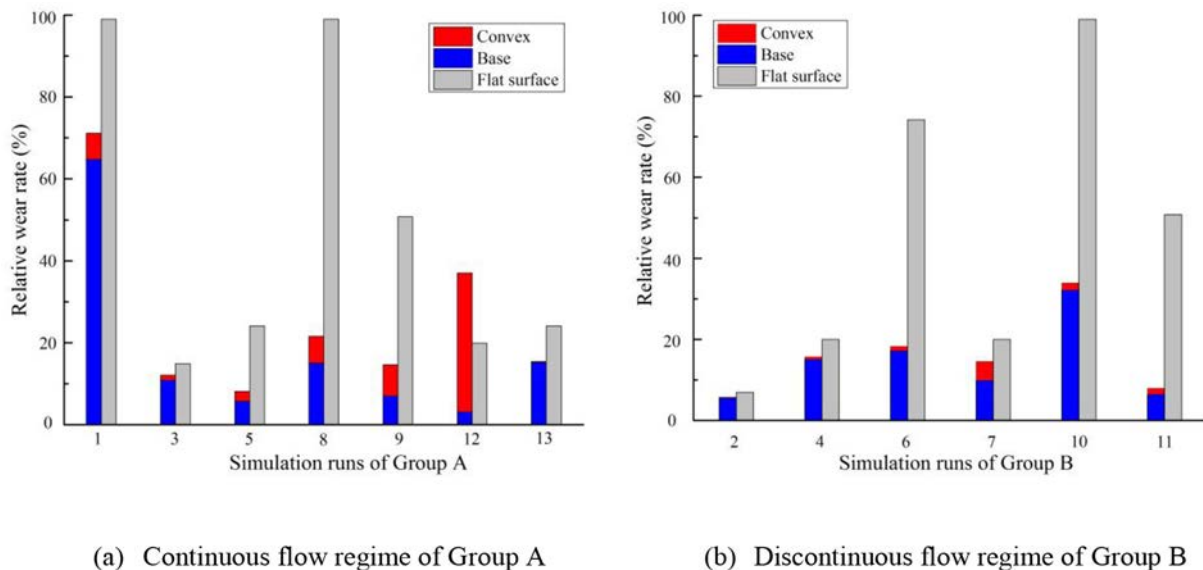

(a) Continuous flow regime of Group A

(b) Discontinuous flow regime of Group B

Fig. 13. Relative wear rate of convex pattern (convex and base) and flat surfaces.

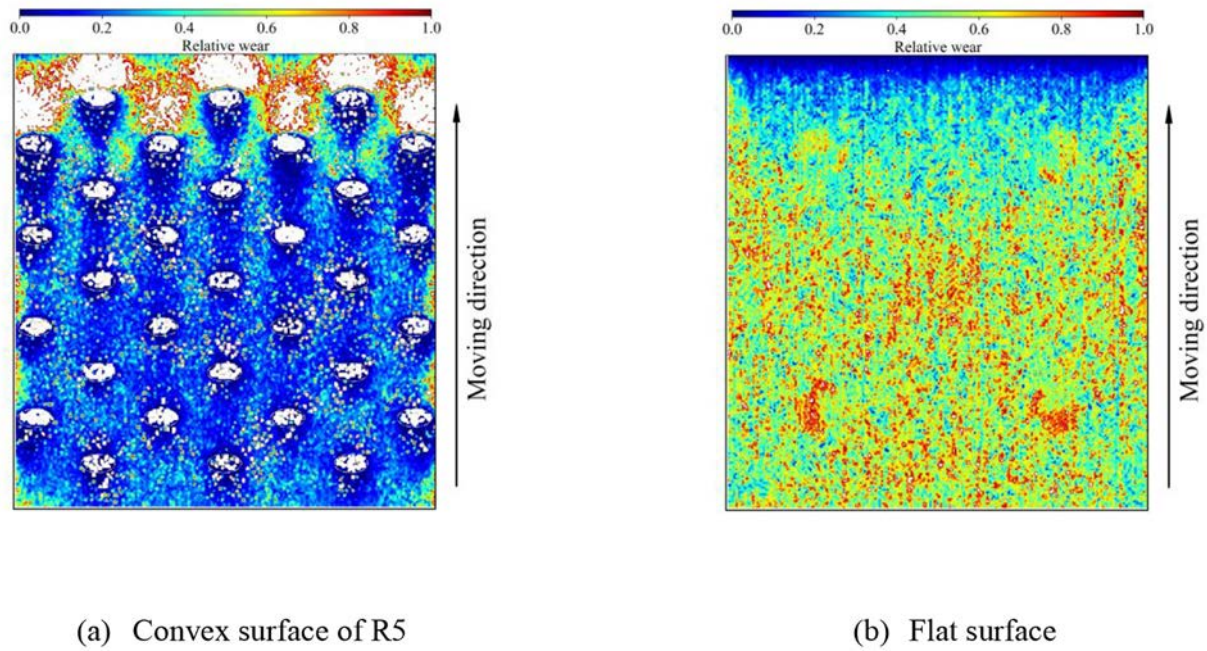(a) Convex surface of R5

(b) Flat surface

Fig. 14. Wear distribution of R5 and the corresponding flat surface (continuous flow regime).

For Fig. 15, R2 shows that the front and the side of the sample suffer the most severe wear, and the sliding wear decreases from the front to the back of the sample. For the corresponding flat surface in Fig. 15(b), the front part of the sample suffers relatively severe wear. It should be noted that the flat surfaces of the corresponding R2 and R5 have different flow regimes which influence the wear distribution of the flat surfaces.

Fig. 16 shows the normal forces of the samples and the error bars represent the fluctuations of the normal force. For the continuous flow regime, the normal forces of the convex pattern samples are higher than that of the flat surfaces except R12, which is consistent

with Fig. 13 (a). Although the normal forces of the convex pattern surfaces are higher than that of the flat surfaces, the relative wear rate is lower, as shown in Fig. 13. With reference to Eq. (6), the sliding wear is linearly related to normal force and sliding distance. Considering the lower wear rate and a similar normal force, this means the sliding distance of the particles on the convex pattern sample is significantly reduced because of the rolling effect of the convexes on particles.

For the discontinuous flow regime, the normal force is relatively comparable between the convex pattern surface and the flat surface except R11. Fig. 13 (b) shows that the convex pattern surfaces have lower
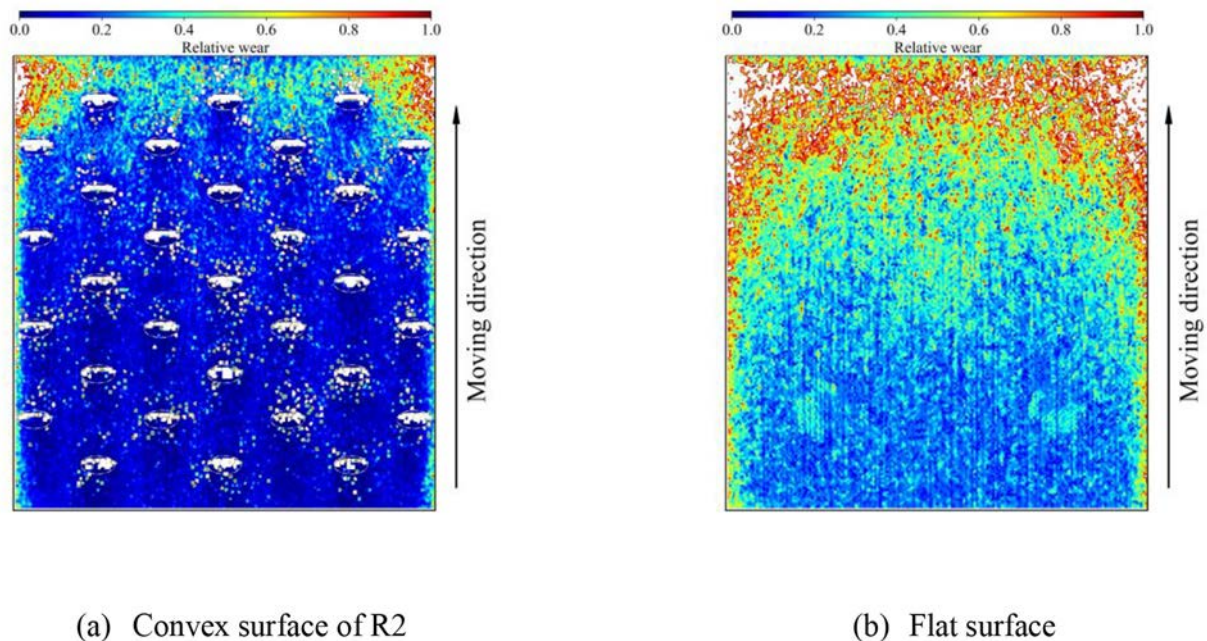

(a) Convex surface of R2

(b) Flat surface

Fig. 15. Wear distribution of R2 and the corresponding flat surface (discontinuous flow regime).
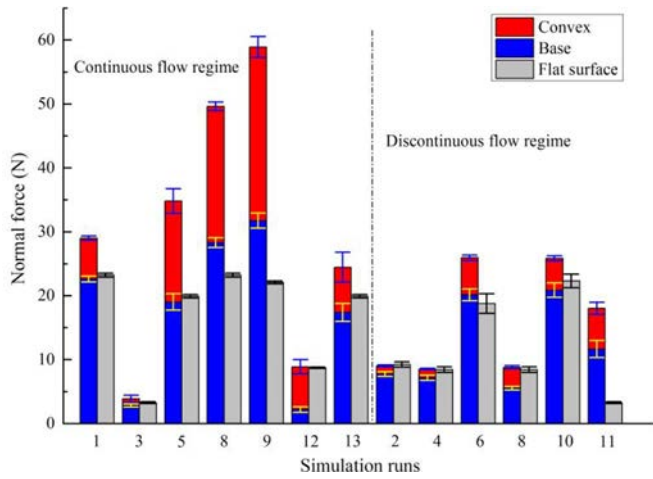
Fig. 16. Normal force of samples.

sliding wear compared with the flat surfaces. On one hand, the rolling effect of the convex pattern reduces the relative sliding between particles and the sample. On the other hand, the corresponding flat surface

may behave continuous flow regime (e.g. R6) which increases the relative sliding distance dramatically and therefore increases the sliding wear rate.

5.3. Bulk property analysis

5.3.1. Bulk flow regimes

The two bulk flow regimes mentioned before are indicated as shown in Fig. 17 and Fig. 18. It should be noted that the colored particles represent the magnitude of angular velocity.

For the continuous flow regime of R5 as shown in Fig. 17 (a), the side view shows that the particles accumulate at the back part of the sample. From the bottom view, it can be seen that the particles around and in front of the sample have higher angular velocity than others. The cross-section view shows a high-side and low-middle particle bed profile, which is because the particles in the accumulation pile flow to the side and are then deposited in the shape, as shown in the cross-section view. The same flow regime appears at the corresponding flat surface, and the particle bed profile is slightly influenced by the flat surface, as shown in Fig. 17 (b). Compared with the bottom view of the flat surface, R5 shows more particles with high angular velocity (red color), and this verifies that the convex pattern surface can facilitate the rolling of particles.
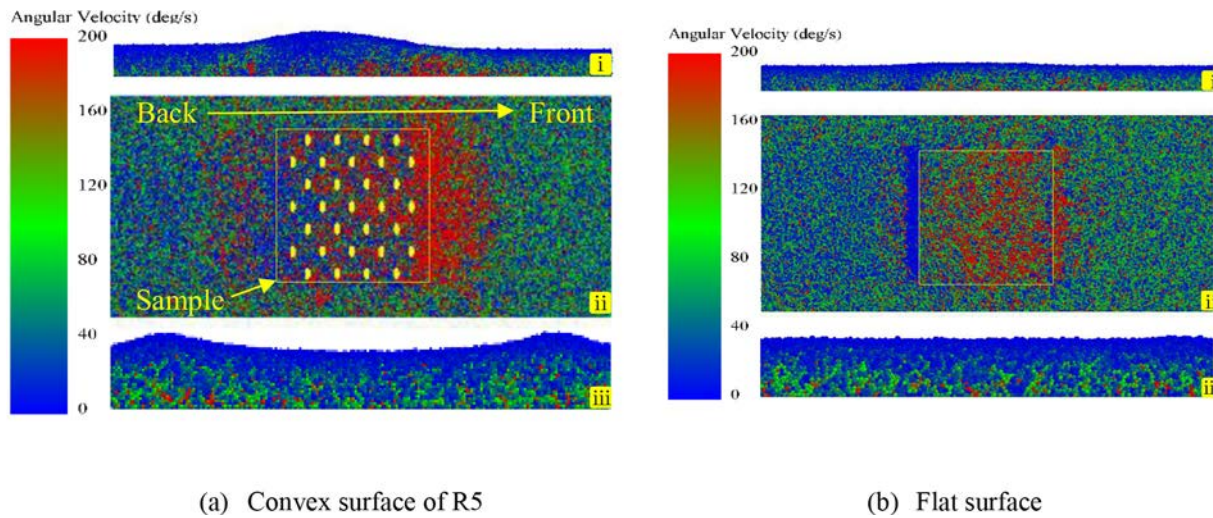

(a) Convex surface of R5   (b) Flat surface

Fig. 17. Continuous flow regime with i) side view (y-z direction clipped from the middle), ii) bottom view (x-y direction) and iii) cross-section view (x-z direction) after passing of the sample.

(a) Convex surface of R2   (b) Flat surface

Fig. 18. Discontinuous flow regime with i) side view (y-z direction clipped from the middle), ii) bottom view (x-y direction) and iii) cross-section view (x-z direction) after passing of the sample.
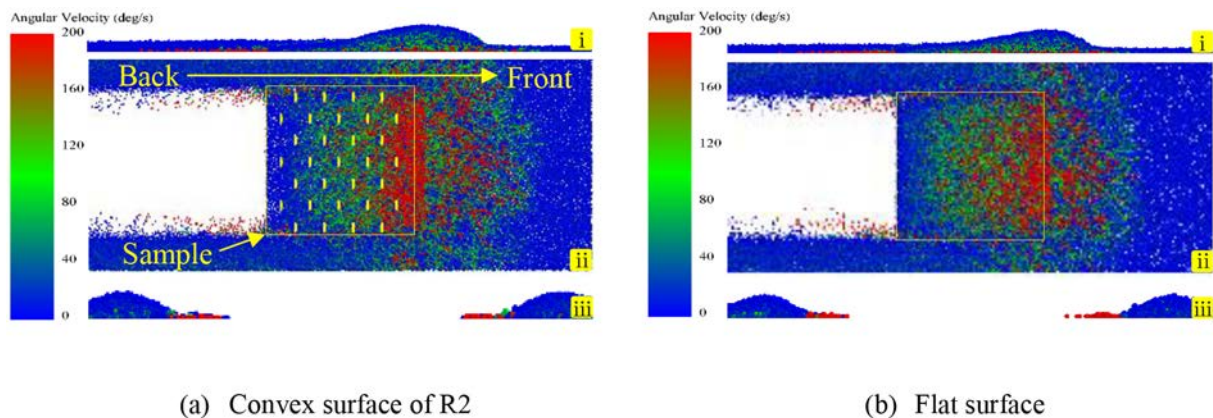
Fig. 18 shows the discontinuous flow regime of R2 and the corresponding flat surface. For R2 in Fig. 18 (a), the accumulation of particles appears in front of the sample, as shown from the side view. The bottom view shows that almost all particles over the sample travel with the sample at the same velocity, and only the particles in front of the sample have relatively high angular velocity. The cross-section view shows a discontinuous particle bed is formed as only the side parts of the particle bed are covered with particles. The corresponding flat surface shows the similar particle bed profile, as shown in Fig. 18 (b). The main reason lies in the influence of the combination between the particle bed thickness and the sample velocity.

5.3.2. Particle velocity profile

Particle velocity profiles of R5 and R2 are used to investigate the influence of the sample on the movement of particles. The profiles include the averaged particle velocity in y-direction, the ratio of the averaged particle velocity in x-direction to that of in y-direction, and the ratio of the averaged particle velocity in z-direction to that of in y-direction. The profiles are based on the moving bins, as illustrated in Fig. 9.

Fig. 19 shows the particle velocity profile of the R5 and the corresponding flat surface. For the averaged particle velocity as shown in

Fig. 19 (a), the particle velocities of R5 are higher than those of the flat surface both in the central and side moving bins from bottom to top layers. For R5, the particle velocity decreases from about 1.5 m/s at layer 1 to 0.4 m/s at layer 8 and keeps around 0.4 m/s for the other layers. The side moving bins show the opposite trend that the averaged velocity lower than 0.1 m/s at the first 8 layers increases slowly, and the velocity reaches more than 0.2 m/s for the rest of the layers. For the flat surface, every layer shows a lower velocity than 0.2 m/s at the central bins, and the particles at the side bins are hardly influenced by the flat surface. It can be seen that the convex pattern sample can significantly influence the movement of particles at the bottom layer. Considering the sample velocity is 2 m/s, Fig. 19 (a) indicates the majority of particles moves much slower than the sample and stays behind the sample, which is consistent with the flow regime, as shown in Fig. 17.

The ratio of the averaged particle velocity in x-direction to that of in y-direction reflects the trend of particles to move sideways. For the central moving bins of R5 as shown in Fig. 19 (b), the velocity ratio is close to 0, which means the tendency of particles to move sideways is negligible. For the side moving bins, the ratio increases from 0.1 to 0.7 at the first 8 layers and decreases to 0.5 at layer 11. This indicates that the particles at the side bins have a strong tendency to move to the sides of the

(a) Average velocity in y direction

(b) Ratio of v_x to v_y
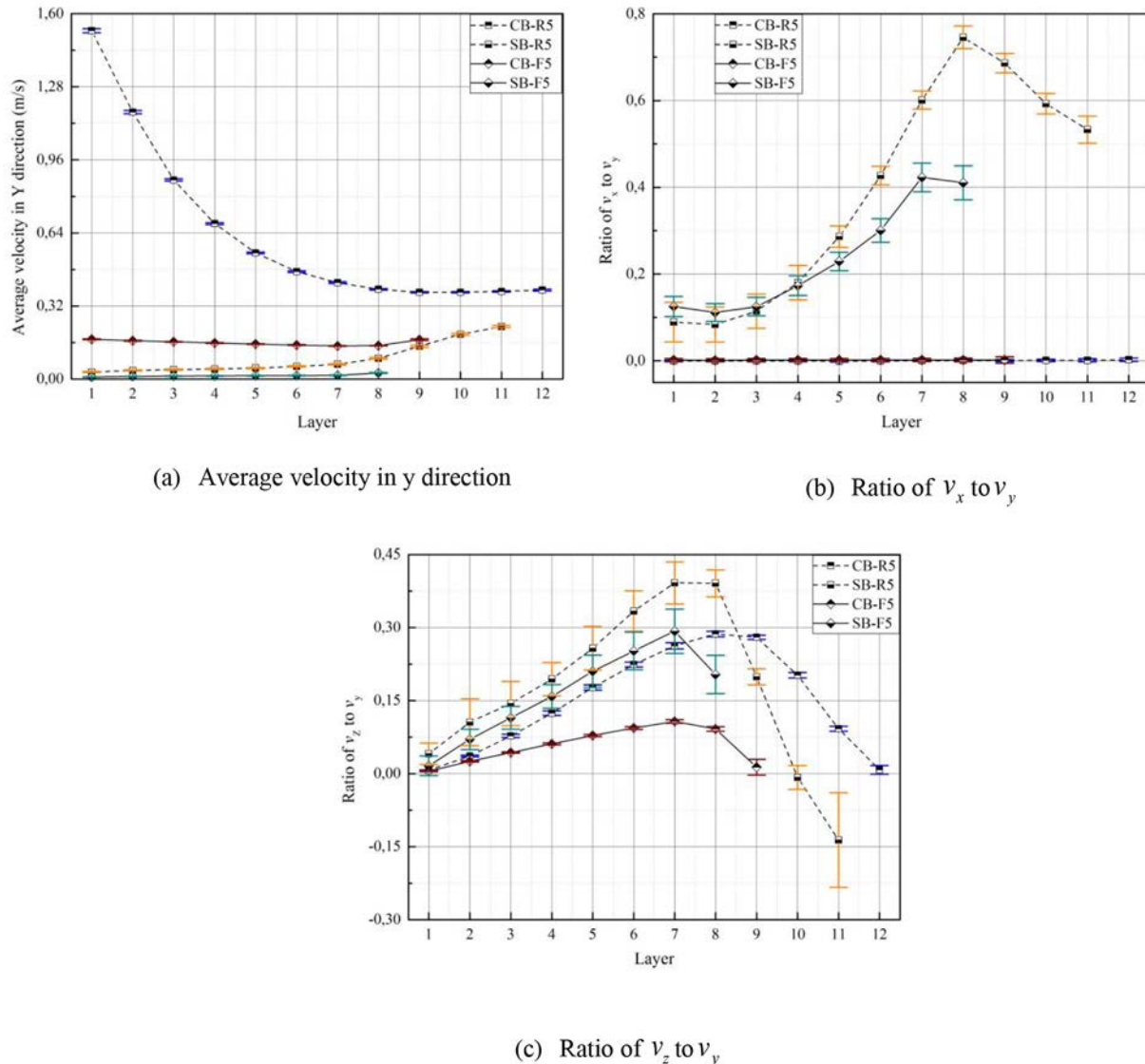
(c) Ratio of v_z to v_y

Fig. 19. Particle velocity profile of R5 and the corresponding flat surface (CB—central moving bins; SB—side moving bins; R5—run 5; F5—flat surface of R5).

particle bed. The reason is that the accumulated particles over the sample are forced to move sideways, and the particles at the bottom layer close to the sides of the sample are pushed sideways. The flat surface shows a similar tendency with R5 both in the central and side bins. For the R5 and the flat surface, all ratios are less than 0.7, which means the particles are more likely to move in the sample moving direction, especially at the central moving bins.

The ratio of the particle velocity in z-direction to that of in y-direction shows the trend of particles to move across layers, as shown in Fig. 19 (c). For the central moving bins of R5, the ratio increases from 0 to near 0.3 at the first eight layers and then decreases to 0 at the top layer. The side bins show the ratio increases to 0.4 at the first eight layers and drop dramatically to below zero. It should be noted that the first eight layers form the original particle bed, and the particle accumulation forces the particles to move vertically, so the first eight layers show the increasing ratio both at the central and side bins. The influence of the sample on the accumulated particles decreases, so the ratio drops from the layer eight to the top layer. The corresponding

flat surface shows the similar trends both at the central and side moving bins.

Fig. 20 shows a similar particle velocity profile of R2 and the corresponding flat surface. For the averaged velocity in y-direction as shown in Fig. 20 (a), the particle velocity for the central moving bins are close to 1 m/s which is the sample velocity. This means the particles are moving forward with the sample at the same velocity. For the side moving bins, the velocity increases slowly at the first two layers from 0.1 m/s to 0.15 m/s and rapidly to close to 0.7 m/s at the top layer. This is because the original particle bed height is 10 mm which fills two layers of the bins, while the other layers are filled by the accumulated particles with high velocity.
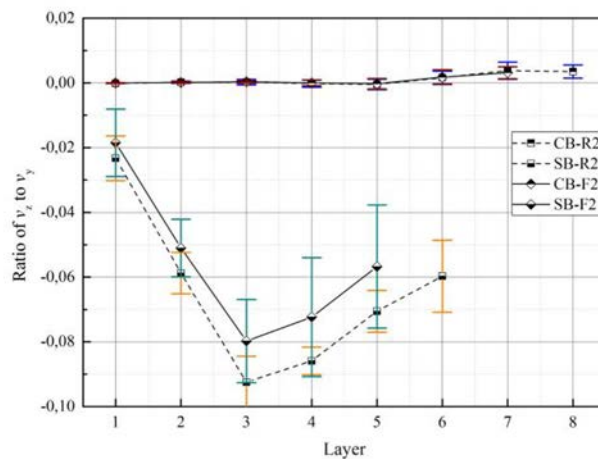
Fig. 20 (b) shows the tendency of particles to move sideways. For the central moving bins, the velocity ratio is close to 0, which indicates the particles at the central moving bins do not tend to move sideways. For the side moving bins, the velocity ratio of the flat surface increases from 0.14 in layer 1 to 0.3 in layer 4 and slightly decreases to 0.27. This shows that the particles in the side moving bins have the tendency
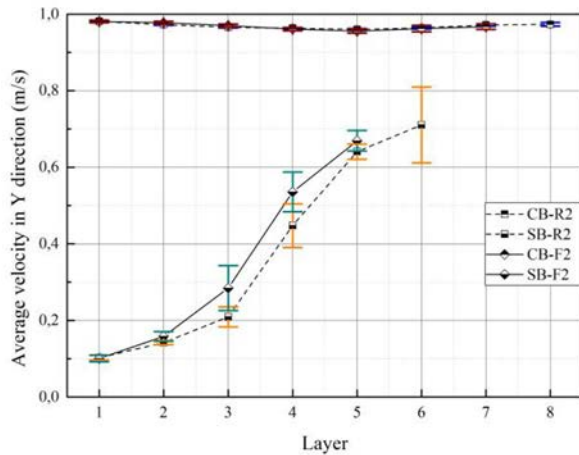
(a) Average velocity in y direction
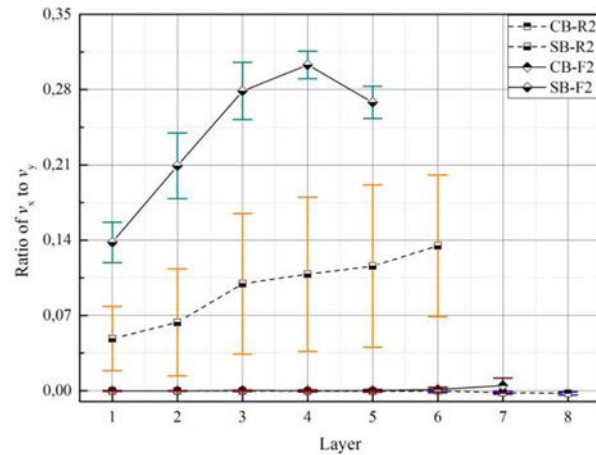
(b) Ratio of v_x to v_y

(c) Ratio of v_z to v_y

Fig. 20. Particle velocity profile of R2 and the corresponding flat surface (CB—central moving bins; SB—side moving bins; R2—run 2; F2—flat surface of R2).

to move sideways, and the trend is stronger at the top layers. For the R2, the ratio increases from 0.05 in the bottom layer to 0.14 in the top layer with a relatively high fluctuation. Although the particles tend to move sideways, the tendency is lower than that of the flat surface.

Fig. 20 (c) shows the tendency of particles to move across layers. For the central moving bins of the R2, the ratio is close to zero, which is because the particles have high velocity in y-direction and make the ratio low. For the side moving bins, the ratio is negative and the absolute value of the ratio increases from 0.02 to 0.09 at the first three layers and decreases to 0.06. The negative value indicates the particles have the tendency to move downwards. The reason lies in that the accumulated particles at the central moving bins are forced to move sideways and downward to side moving bins. The corresponding flat surface shows the similar trend both at the central and side moving bins.

5.3.3. Particle angular velocity profile

The particle angular velocity profile shows the magnitude of the averaged angular velocity and reflects the rolling effect of the convex pattern, as the rolling instead of sliding of particles is the main mechanism of reducing the sliding wear.

Fig. 21 shows the similar trend of particle angular velocity of R5 and the corresponding flat surface. The angular velocity decreases from bottom layer to top layer and the particles at the central moving bins have higher angular velocities than those of at the side moving bins. The side moving bins for both the R5 and the flat surface have the angular velocity of lower than 120 deg./s. For the central moving bins, the top layer of the R5 has the highest value of higher than 320 deg./s which is two times higher than that of the flat surface. The angular velocity drops dramatically from the first layer to the second layer and this means the convex pattern surface can induce the rolling and reduce the sliding of particles contacting with the convex pattern. (See Fig. 22.)

R2 and the corresponding flat surface show the similar trend of the angular velocity for both the central and side moving bins. This indicates the convex pattern surface can hardly influence the motion of the particles at the discontinuous flow regime, and the flow regime dominates the motion of particles.

5.3.4. Discussion

The bulk flow regimes have significant influence on the motion of particles and determine the mechanisms of the reduction of the sliding wear. The convex pattern surface can convert the sliding of particles to the rolling of particles at the continuous flow regime. The discontinuous
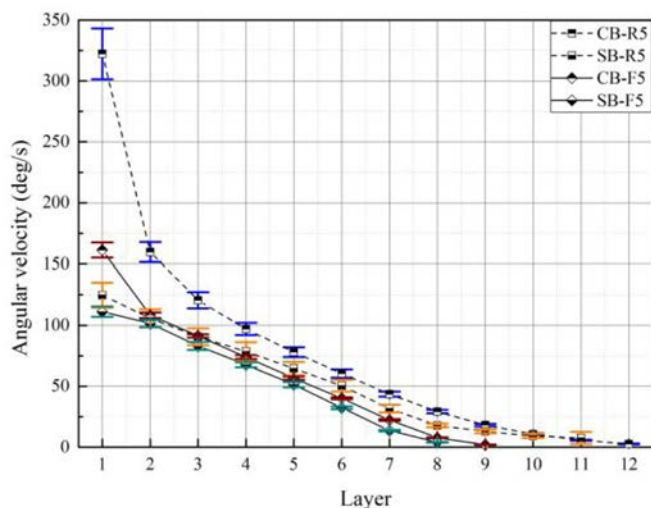

Fig. 21. Angular velocity profile of R5 and the corresponding flat surface (CB—central moving bins; SB—side moving bins; R5—run 5; F5—flat surface of R5).
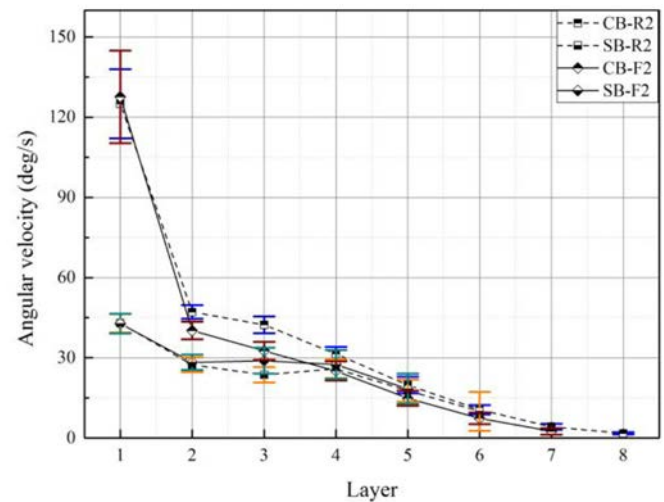

Fig. 22. Angular velocity profile of R2 and the corresponding flat surface (CB—central moving bins; SB—side moving bins; R2—run 2; F2—flat surface of R2).

Table 9
Regression equation of fitted model.

Response	Regression equation in coded units	R^2	R^2(adj)	R^2(pred)
$\ln(y)$	$y = -1.859 + 0.449a + 0.650v + 1.425t - 0.629b \times d$	95%	92%	86%

flow regime reduces the relative motion between particles and the sample to reduce the sliding distance and therefore leads to severe particle accumulation. Compared with the flat surface, the convex pattern has slight influence on the rolling of particles at the discontinuous flow regime.

5.4. DSD analysis

To quantify the effect of the factors tested, a regression equation is fitted based on normalized wear results which are divided by the highest value of the wear volumes. Table 9 lists the fitted model and the corresponding R^2. It should be noted that the fitted model is non-hierarchical because it does not contain all of the lower order terms (factor b and d) for each term (interaction $b \times d$) in the model, so this model is fitted in coded unit logarithm $\ln(y)$ [46]. The model indicates that three main factors and one two-level interaction have significant influence on the sliding wear volume. The R^2 value of more than 95% indicates the model provides a good fit to the data points, and the adjusted and predicted R^2 with relative high values also manifest the goodness of the model.

A significance level of 0.05 (α) is chosen in this design to compare a p-value to assess the significance of the terms. As listed in Table 10, the p-values of the coefficients of the constant, a,v,t, and the interaction $b \times d$ are lower than 0.05, which means there is a statistically significant association between the sliding wear volume and the terms of the

Table 10
Coefficients of the regression equation and the corresponding p-value.

Term	Coefficient	P-value
Constant	−1.859	0.000
a	0.448	0.032
v	0.650	0.007
t	1.426	0.000
$b \times d$	−0.633	0.013

Fig. 23. Residual plot.

(a)　Major radius and particle bed thickness

(b)　Major radius and sample velocity

(c)　Sample velocity and particle bed thickness

(d)　Minor radius and horizontal distance
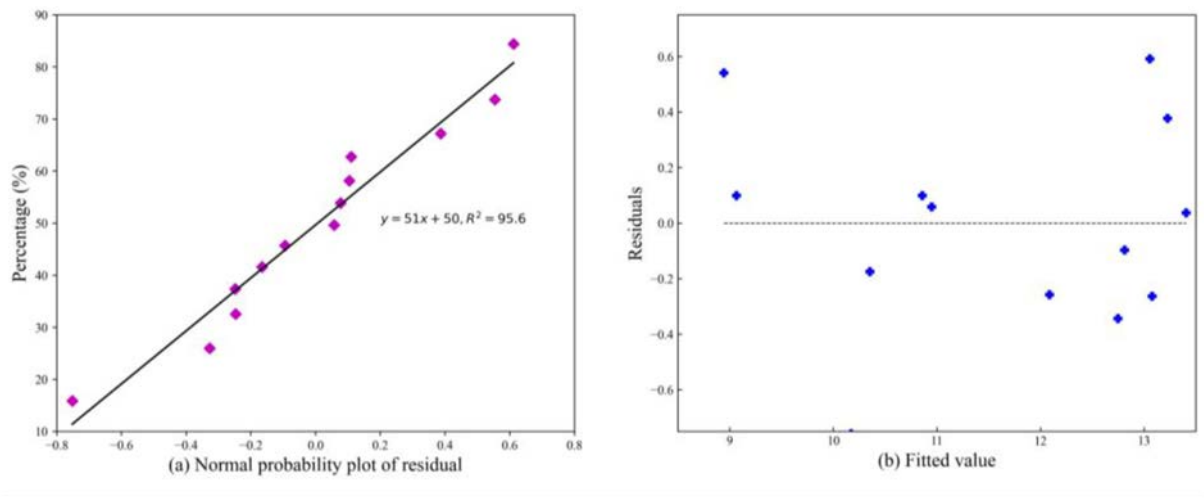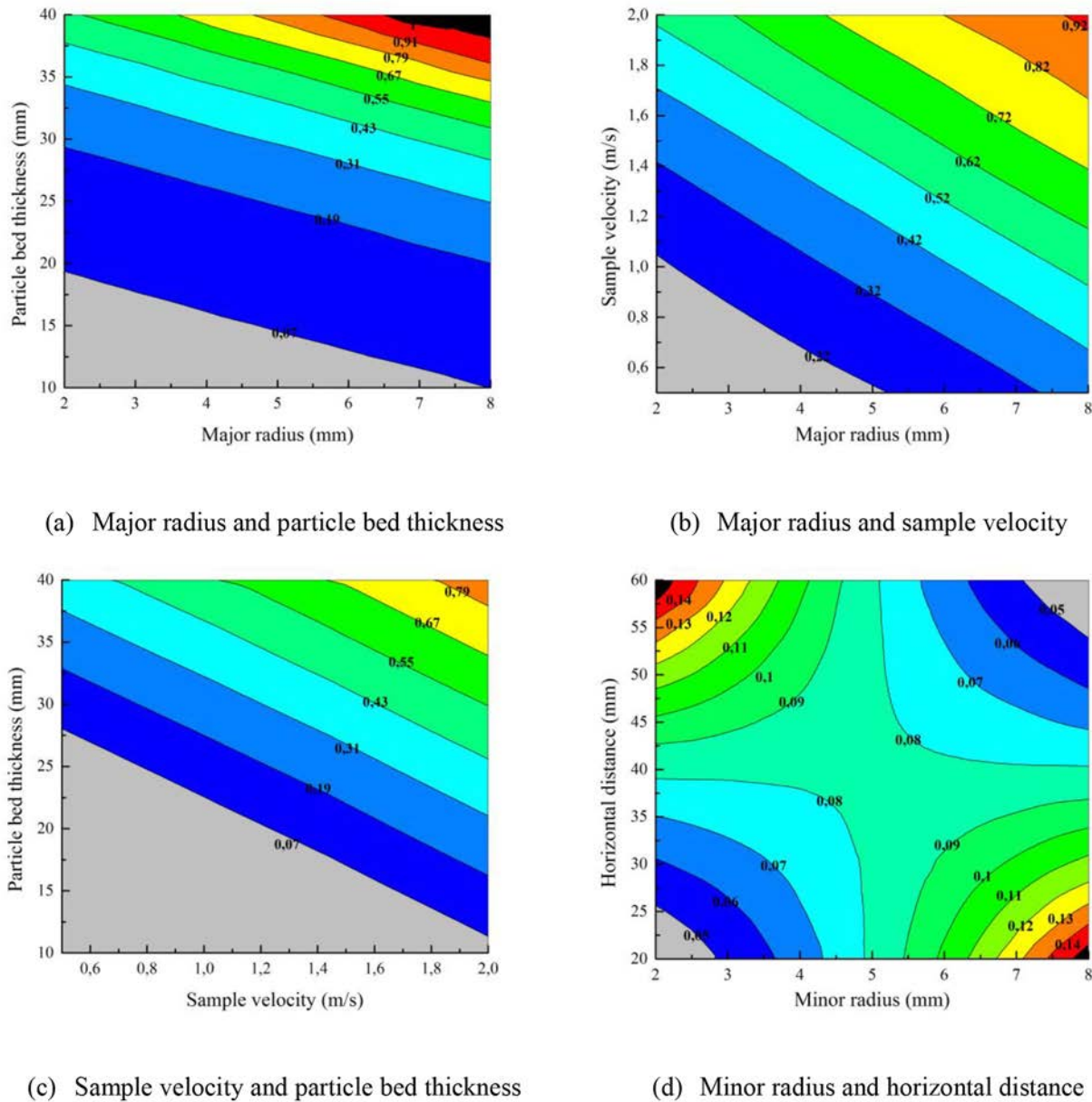
Fig. 24. Normalized response contour plot.

regression equation. The higher the coefficient of a factor is, the more important the factor is on the effect of the sliding wear. Therefore, the particle bed thickness has the most significant effect on the response, while the major radius has the least. In addition, the sample velocity and the interaction between the minor radius and the horizontal distance show a comparable influence on the sliding wear.

A residual plot as shown in Fig. 23 is used to determine whether the fitted model is adequate and meets the assumptions of the analysis. The normal probability plot of residuals, as shown in Fig. 23 (a) displays the relation between residuals and the expected values when the distribution is normal and verifies that the residuals are normally distributed as the plot of the residuals approximately follow a straight line. Fig. 23 (b) demonstrates the relation between residuals and fitted values of response (normalized wear volume), which is used to verify the assumption that the residuals are randomly distributed with a relatively constant variance. It can be seen that the points fall randomly on both sides of 0 with no recognizable patterns in the points. Based on the analysis of the residual plots, it can be concluded that the regression model meets the assumption (listed in Table 9).

A contour plots Fig. 24 is used to express the relationship between two factors and the normalized response values, while the other factors are kept at the middle level. For a specific wear volume, the three main factors show the negative linear correlations each other, which means the increase of one factor leads to the decrease of another factor. For Fig. 24 (a), it can be seen that the major radius has a small effect on the sliding wear volume compared with the particle bed thickness. Fig. 24 (b) shows that the influence of the major radius and the sample velocity is similar which is consistent with the analysis of model coefficients. Fig. 24 (c) reveals the sliding wear volume is linearly related to the particle bed thickness. The interaction between the minor radius and the horizontal distance is shown in Fig. 24 (d). The curvature expresses the influence of one factor depends on another. As shown in Fig. 24 (d), the sliding wear volume is low when both the minor radius and the horizontal distance have low or high levels at the same time.

6. Conclusions

This work entails detailed investigations of bulk flow regimes and sliding wear mechanisms of the convex pattern and flat surfaces. The aim of this work focuses on the optimization of a convex pattern surface to reduce the sliding wear caused by non-cohesive free flowing bulk material. Three conclusions can be drawn:

1) Two flow regimes are formed, namely, the continuous and discontinuous flow regime, and the mechanisms of the sliding wear reduction for the two flow regimes are different. For the continuous flow regime, the convex pattern surface can significantly increase the rolling of particles to reduce the relative sliding between particles and the sample. The discontinuous flow regime can reduce the sliding distance dramatically, and the convex pattern has slight rolling effect on the particles. The continuous flow regime is preferred, as this flow regime induces less particle accumulation and more apparent rolling effect of particles.

2) Three main factors and one interaction have statistical significance based on the regression model. The particle bed thickness has the most significant influence on the sliding wear, and the flow regime is continuous when the particle bed thickness is 40 mm. The height and the minor radius of the convex have no significant influence on the sliding wear, which is consistent with the previous study.

3) R5 and R2 are the optimal design for the continuous and discontinuous flow regimes, respectively. The properties of the two runs hint to a design that is optimal in both regimes simultaneously. It should be noted that this optimal design is based on the specific dry bulk material with d_{50} of 2.65 mm, and it is suitable for bulk material with similar bulk properties.

Future work will focus on the robustness of the optimal convex pattern surfaces by investigating the influence of particle size and shape on the sliding wear. The relationship between particle size and the dimensions of the optimal convex pattern will be clarified, and the rolling effect of the convex pattern on non-spherical particles will be elaborated. Additionally, the wear reduction performance of optimal design R5 will be extensively tested in an experimental setup to validate the numerical findings described in this paper.

Formatting of funding resources

Declaration of Competing Interest

This paper has no conflict of interest.

Appendix A

Wear distributions (Fig. 14) show that the front part of the convex pattern sample has significantly more sliding wear than the back part. However, on the contrary, the front part of the flat surface shows less sliding wear compared with the back part. Based on Archard wear model denoted in Eq. (6), the sliding wear is determined by sliding distance and normal force when other parameters are remained constant. In order to investigate the normal force and sliding distance, a bin group as shown in Fig. A.1 is used. The bin group consists of 10 bins and each bin measures $200mm \times 20mm \times 5mm$ as only the bottom layer of particles determines the sliding distance. The sliding distance is directly related to velocity difference between particles and the sample, so a relative velocity difference is used to replace sliding distance, and the higher the relative velocity difference is, the longer the sliding distance
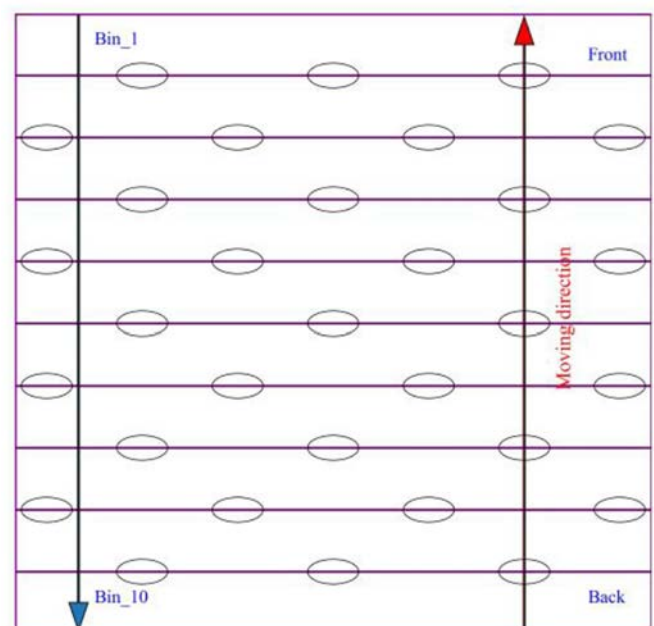

Fig. A.1. Bin group.

Relative velocity difference is denoted as Eq. (A.1)

$$\alpha = \frac{\left| v_{sample} - \overline{v_{particle}} \right|}{\left| v_{sample} \right|} \times 100\%$$ (A.1)

where α is relative velocity difference; v_{sample} is the sample velocity; $\overline{v_{particle}}$ is the averaged sliding velocity of particles in each bin.

For the flat surface (F5) as shown in Fig. A.2, the relative velocity difference for all bins is between 91% and 94%, which means the sliding distance of particles in each bin is comparable. Fig. A.3 shows the normal force of the flat surface increases from 0.7 N at bin 1 to 2.1 N at bin 4 and maintains a relatively stable value until bin 10. This indicates that the contact between particles and the flat sample at the first four bins is at transition state. This is because the contact number between particles and the sample as shown in Fig. A.4 is much lower than that of the rest bins where the contact number is relatively comparable. Based on the combination of the sliding distance and normal force, it can conclude that the sliding wear increases from bin 1 to bin 4 and maintains a comparable value until bin 10, and this analysis is consistant with the wear distribution as shown in Fig. 14 (b).

For the convex pattern surface (R5), the relative velocity difference as shown in Fig. A.2 drops dramatically from 78% at bin 1 to 16% at bin 6 and rises to 30% at bin 10, which means the front rows of convexes force the particle flow passing by to be changed abruptly to deflect the bulk flow behavior, while the back rows do not have to deal with a change in bulk flow until bin 8. In addition, the particles at the back rows move with the sample because of the low relative velocity difference, so the sliding distance is much lower than that of the front rows. For the normal force as shown in Fig. A.3, all bins show higher normal force than that of the flat surface which is because the total normal force is consists of the gravity of particles on the base of the sample and the normal force on the convex pattern. With the decrease of the relative velocity difference, the normal force drops from bin 2 to bin 6 because the lower relative velocity difference means the particles are moving with the sample and the contact force between particles, and the convex pattern reduces. Although the normal force increases to a highest value of 6 N at bin 8, the sliding distance is much lower than that of the bin 1, so the sliding wear is lower. The contact number as shown in Fig. A.4 has an opposite trend to the relative velocity difference because of the change in bulk flow behavior. Based on the analyses above, it can be explained that the front part of the convex pattern surface suffers more severe sliding wear.
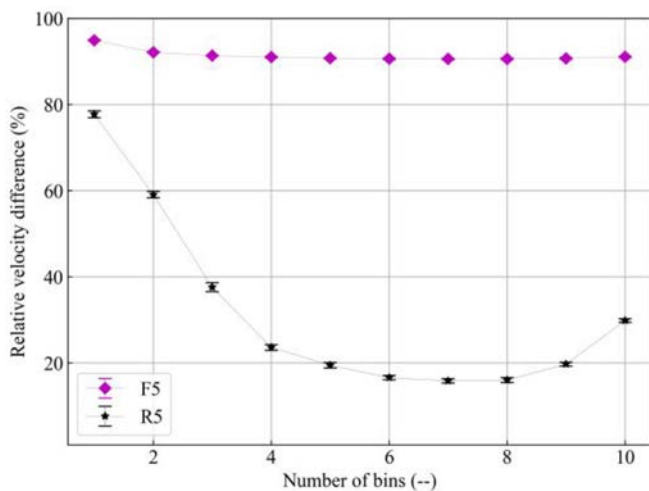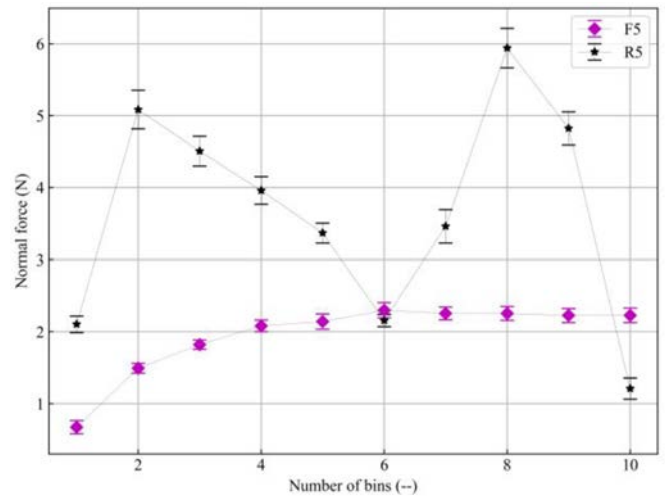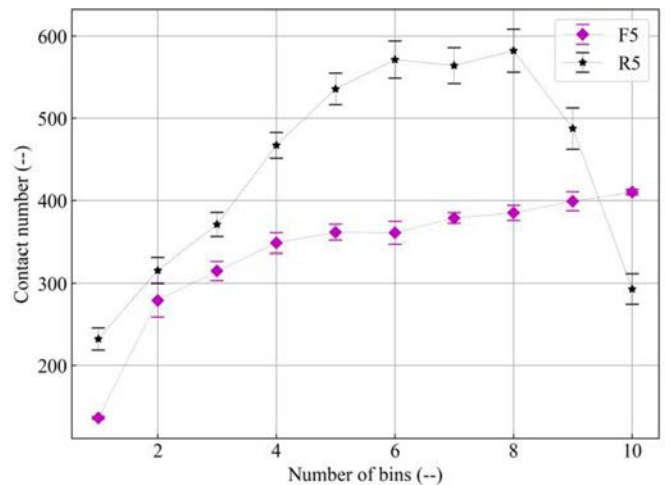

Fig. A.3. Normal force.

Fig. A.4. Contact number between particles and sample.

References

[1] D. Schulze, Powders and Bulk Solids: Behaviour, Characterization, Storage and Flow, Springer, 2008.

[2] A.W. Roberts, M. Ooms, S. Wiche, Concepts of boundary friction, adhesion and wear in bulk solids handling operations, Proc. Third International Conference on Bulk Materials, Storage, Handling and Transportation, Newcastle, NSW, Australia, 1989.

[3] K.R.G. Tuckey, Intelligent selection of engineered wear linings in iron ore plant, Miner. Process. Ext. Metall. 112 (2003) 33–38, https://doi.org/10.1179/037195503225011420.

[4] A.W. Roberts, Chute performance and design for rapid flow conditions, Chem. Eng. Technol. 26 (2003) https://doi.org/10.1002/ceat.200390024.

[5] M. Andrejiova, A. Grincova, D. Marasova, Measurement and simulation of impact wear damage to industrial conveyor belts, Wear. 368–369 (2016) 400–407, https://doi.org/10.1016/j.wear.2016.10.010.

[6] G. Chen, D.L. Schott, G. Lodewijks, Bionic design methodology for wear reduction of bulk solids handling equipment, Part. Sci. Technol. 35 (2017) 525–532, https://doi.org/10.1080/02726351.2016.1144666.

[7] A.W. Roberts, S.J. Wiche, Prediction of lining wear life of bins and chutes in bulk solids handling operations, Tribol. Int. 26 (1993) 345–351, https://doi.org/10.1016/0301-679X(93)90071-8.

[8] P. Hilgraf, Wear in bulk materials handling, Bulk Solids Handl. 27 (2007) 179–187.

[9] L. Ren, Progress in the bionic study on anti-adhesion and resistance reduction of terrain machines, Sci. China Ser. E Technol. Sci. 52 (2009) 273–284, https://doi.org/10.1007/s11431−009-0042-3.

[10] J.F.V. Vincent, O.A. Bogatyreva, N.R. Bogatyrev, A. Bowyer, A.K. Pahl, Biomimetics: its practice and theory, J. R. Soc. Interface 3 (2006) 471–482, https://doi.org/10.1098/rsif.2006.0127.

[11] G. Chen, Surface Wear Reduction of Bulk Solids Handling Equipment Using Bionic Design, 2017 https://doi.org/10.4233/uuid:b60cb231-222d-434d-b987-cf36605bc719.

Fig. A.2. Relative velocity difference.

[12] J. Tong, T. Biao Lü, Y. Hai Ma, H. Kun Wang, L. Quan Ren, R.D. Arnell, Two-body abrasive wear of the surfaces of pangolin scales, J. Bionic. Eng. 4 (2007) 77–84, https://doi.org/10.1016/S1672-6529(07)60017-1.

[13] L. Ren, J. Tong, S. Zhang, B. Cheng, Reducing sliding resistance of soil against bulldozing plates by unsmoothed bionics surfaces, J. Terrramech. 32 (1995) 303–309, https://doi.org/10.1016/0022-4898(96)00001-8.

[14] A. Filippov, S.N. Gorb, Frictional-anisotropy-based systems in biology: structural diversity and numerical model, Sci. Rep. 3 (2013) 1–6, https://doi.org/10.1038/srep01240.

[15] G. Ke, S. Youhong, G. Runfeng, X. Liang, W. Chuanliu, L. Yumin, Application and prospect of bionic non-smooth theory in drilling engineering, Pet. Explor. Dev. 36 (2009) 519–522,541, https://doi.org/10.1016/S1876-3804(09)60143-9.

[16] A. Singh, E.-S. Yoon, Biomimetics in tribology - recent developments, J. Korean Phys. Soc. 52 (2008) https://doi.org/10.3938/jkps.52.656.

[17] C. Greiner, M. Schäfer, Bio-inspired scale-like surface textures and their tribological properties, Bioinspir. Biomimet. 10 (2015) https://doi.org/10.1088/1748-3190/10/4/044001.

[18] Y. Yan, W. Vreeburg, G. Chen, D. Schott, Minimization of wear in a transfer chute by geometric optimization of convex pattern surface: a DEM study, Proc. 8th International Conference on Discrete Element Methods, Twente, The Netherlands, 2019.

[19] Y. Yan, W. Vreeburg, G. Chen, C. Wheeler, D. Schott, Design of optimized convex pattern surface for wear tests in a test rig, Proc: 13th International Conference on Bulk Materials Storage, Handling and Transportation, Mantra, Queensland, Australia, 2021.

[20] P. Cundall, O. Strack, A discrete numerical model for granular assemblies, Geotechnique 29 (1979) 47–65, https://doi.org/10.1680/geot.1979.29.1.47.

[21] C.J. Coetzee, Review: calibration of the discrete element method, Powder Technol. 310 (2017) 104–142, https://doi.org/10.1016/j.powtec.2017.01.015.

[22] L. Zhao, X. Liu, J. Mao, D. Xu, A. Munjiza, E. Avital, A novel discrete element method based on the distance potential for arbitrary 2D convex elements, Int. J. Numer. Methods Eng. 115 (2018) 238–267, https://doi.org/10.1002/nme.5803.

[23] R.D. Mindlin, Elastic spheres in contact under varying oblique forces, J. Appl. Mech. 20 (1953) 327–344, https://doi.org/10.1007/978-1-4613-8865-4_35.

[24] EDEM Simulation, EDEM 2018 Theory Reference Guide, DEM Solutions, 2018.

[25] C. Thornton, Interparticle sliding in the presence of adhesion, J. Phys. D. Appl. Phys. 24 (1991) 1942–1946, https://doi.org/10.1088/0022-3727/24/11/007.

[26] S.M. Derakhshani, D.L. Schott, G. Lodewijks, Micro-macro properties of quartz sand: experimental investigation and DEM simulation, Powder Technol. 269 (2015) 127–138, https://doi.org/10.1016/j.powtec.2014.08.072.

[27] P.M. Esteves, D.B. Mazzinghy, R. Galéry, L.C.R. Machado, Industrial vertical stirred mills screw liner wear profile compared to discrete element method simulations, Minerals. 11 (2021) 1–20, https://doi.org/10.3390/min11040397.

[28] L. Xu, K. Luo, Y. Zhao, Numerical prediction of wear in SAG mills based on DEM simulations, Powder Technol. 329 (2018) 353–363, https://doi.org/10.1016/j.powtec.2018.02.004.

[29] D. Boemer, J.P. Ponthot, A generic wear prediction procedure based on the discrete element method for ball mill liners in the cement industry, Miner. Eng. 109 (2017) 55–79, https://doi.org/10.1016/j.mineng.2017.02.014.

[30] M.S. Powell, N.S. Weerasekara, S. Cole, R.D. Laroche, J. Favier, DEM modelling of liner evolution and its influence on grinding rate in ball mills, Miner. Eng. 24 (2011) 341–351, https://doi.org/10.1016/j.mineng.2010.12.012.

[31] C.M. Wensrich, A. Katterfeld, Rolling friction as a technique for modelling particle shape in DEM, Powder Technol. 217 (2012) 409–417, https://doi.org/10.1016/j.powtec.2011.10.057.

[32] C.J. Coetzee, Calibration of the discrete element method and the effect of particle shape, Powder Technol. 297 (2016) 50–70, https://doi.org/10.1016/j.powtec.2016.04.003.

[33] J. Ai, J.F. Chen, J.M. Rotter, J.Y. Ooi, Assessment of rolling resistance models in discrete element simulations, Powder Technol. 206 (2011) 269–282, https://doi.org/10.1016/j.powtec.2010.09.030.

[34] Y.C. Zhou, B.D. Wright, R.Y. Yang, B.H. Xu, A.B. Yu, Rolling friction in the dynamic simulation of sandpile formation, Phys. A: Statist. Mech. Appl. 269 (1999) 536–553, https://doi.org/10.1016/S0378-4371(99)00183-1.

[35] J.F. Archard, Contact and rubbing of flat surfaces, J. Appl. Phys. 24 (1953) 981–988, https://doi.org/10.1063/1.1721448.

[36] X. Qui, A. Potapov, M. Song, L. Nordell, Prediction of Wear of Mill Lifters Using Discrete Element Method, 2001 2–7 ImpactoRecub.

[37] D. Forsström, P. Jonsén, Calibration and validation of a large scale abrasive wear model by coupling DEM-FEM: local failure prediction from abrasive wear of tipper bodies during unloading of granular material, Eng. Fail. Anal. 66 (2016) 274–283, https://doi.org/10.1016/j.engfailanal.2016.04.007.

[38] T. Roessler, C. Richter, A. Katterfeld, F. Will, Development of a standard calibration procedure for the DEM parameters of cohesionless bulk materials – part I: solving the problem of ambiguous parameter combinations, Powder Technol. 343 (2019) 803–812, https://doi.org/10.1016/j.powtec.2018.11.034.

[39] Y.C. Zhou, B.H. Xu, A.B. Yu, P. Zulli, An experimental and numerical study of the angle of repose of coarse spheres, Powder Technol. 125 (2002) 45–54, https://doi.org/10.1016/s0032-5910(01)00520-4.

[40] ANSYS Inc, ANSYS Help 18.2, ANSYS Inc Canonsburg, 2018.

[41] M.S. Bingley, S. Schnee, A study of the mechanisms of abrasive wear for ductile metals under wet and dry three-body conditions, Wear. 258 (2005) 50–61, https://doi.org/10.1016/j.wear.2004.01.022.

[42] I.M. Hutchings, P. Shipway, Tribology: Friction and Wear of Engineering Materials, Butterworth-Heinemann, 2017.

[43] T. Deng, M.S. Bingley, M.S.A. Bradley, The influence of particle rotation on the solid particle erosion rate of metals, Wear. 256 (2004) 1037–1049, https://doi.org/10.1016/S0043-1648(03)00536-2.

[44] D.C. Montgomery, Design and Analysis of Experiments, 9th ed. John Wiley & Sons, 2017.

[45] B. Jones, C.J. Nachtsheim, A class of three-level designs for definitive screening in the presence of second-order effects, J. Qual. Technol. 43 (2011) 1–15, https://doi.org/10.1080/00224065.2011.11917841.

[46] , Available at https://support.minitab.com/en-us/minitab/19/help-and-how-to/statistical-modeling/doe/how-to/screening/analyze-screening-design/perform-the-analysis/non-hierarchical-model/.